X-ray resonant magnetic scattering from patterned multilayers

Unnar B. Arnalds,[1] Thomas P. A. Hase,[2] Evangelos Th. Papaioannou,[1] Hossein Raanaei,[3] Radu Abrudan,[4] Timothy R. Charlton,[5] Sean Langridge,[5] and Björgvin Hjörvarsson[1]

[1]*Department of Physics and Astronomy, Uppsala University, Box 530, S-751 21 Uppsala, Sweden*

[2]*Department of Physics, University of Warwick, Coventry CV4 7AL, United Kingdom*

[3]*Department of Physics, Persian Gulf University, Bushehr 75169, Iran*

[4]*Ruhr-Universität Bochum, D-44780 Bochum, Germany*

[5]*ISIS, Rutherford Appleton Laboratory, Harwell Science and Innovation Campus, Didcot, Oxfordshire OX11 0QX, United Kingdom*

(Received 17 March 2012; revised manuscript received 5 July 2012; published 20 August 2012)

We report on x-ray resonant magnetic scattering from laterally patterned arrays of amorphous $Co_{68}Fe_{24}Zr_8/Al_2O_3$ multilayers. The arrays are composed of circular and ellipsoidal elements which display distinct individual magnetic responses enabling the investigation of the dependence of the observed magnetization on the scattering condition. We focus our attention to special points in reciprocal space, relating to the lateral and perpendicular structure of the samples, thereby revealing the magnetic structure of the multilayered arrays. This allows a comparison of the observed magnetization under different scattering conditions to magneto-optical measurements. The scattering data are supported by micromagnetic simulations which further enhance our understanding of the intricate charge and magnetic scattering from three dimensional patterns.

DOI: 10.1103/PhysRevB.86.064426 PACS number(s): 75.25.−j, 75.70.Ak, 68.65.Ac, 75.60.Jk

I. INTRODUCTION

Since the time of Faraday and Kerr, polarized light has been used to elucidate the magnetic properties of materials.[1] More recently this approach has been adopted at x-ray energies making use of resonant magnetic scattering (XRMS)[2] at synchrotron sources which brings the added advantage of element specificity to the analysis.[3] The element specificity is obtained by the choice of the energy of the synchrotron radiation (SR) which is tuned to match the core energy levels of the element of interest. As with optical wavelengths, the magnetic contribution to the scattered intensity can be studied using polarized x-rays. The spatially resolved magnetic structure of artificially created thin films and multilayers can be investigated by studying the distribution of the scattered intensity in reciprocal space. By selecting suitable experimental geometries the scattering becomes sensitive to specific periodicities within the sample enabling the magnetization to be studied over particular length scales and directions.[4–8]

With the advent of controllable lateral patterning techniques,[9,10] additional dimensions have been brought into consideration for the design of future applications. In arrays of a single material the main control parameters available for tailoring the macroscopic properties are the element shape and array parameters which modify interdot interactions. In patterned multilayers additional intra-element interactions such as interlayer coupling and dipole interactions between layers increases the complexity of the magnetic ground state thereby increasing the range of possible applications.

To realize the potential of patterned materials, characterization techniques that are sensitive to the periodicities in these array samples are required. In-plane diffraction measurements offer the possibility of both measuring the magnetic correlations and determining the lateral and perpendicular magnetic periodicities.[11] Both in-plane and out-of-plane periodicities within the sample give rise to Bragg peaks at well-defined positions in reciprocal space. From their location, intensity, and shape as a function of an applied field the three-dimensional magnetic structure can be determined and compared directly with the chemical structure in arrays with hugely varying length scales.[12–14]

In this paper we move towards utilizing the unique possibility of XRMS to explore the magnetization and its reversal in patterned multilayers composed of differently shaped elements on a rectangular array. We investigate the magnetic behavior of the structures and reveal the dependence of the observed magnetization on the scattering condition highlighting the difference between optical and x-ray probes.

II. EXPERIMENT

A. Sample preparation

Multilayered structures consisting of ten repetitions of amorphous 3-nm thick $Co_{68}Fe_{24}Zr_8$ and 3-nm thick Al_2O_3, seeded and terminated with an Al_2O_3 layer, were prepared by magnetron sputtering onto prepatterned Si substrates.[15–17] After growth a chemical liftoff process was used to obtain the final patterned multilayer structures. The sample preparation has been described previously in detail.[14] The large area patterns ($\sim$1 cm^2) consist of different spatial configurations of 1.5 μm diameter circular and 1.5 μm $\times$ 4.5 μm ellipsoidal islands. The shape anisotropy of the films gives rise to an in-plane magnetization and a magnetic field applied during growth sets a uniaxial magnetic anisotropy in the elements aligned to the major axis of the ellipses. Atomic force microscopy (AFM) images of the two patterned arrays are depicted in Fig. 1. The measured nearest-neighbor distance between the ellipses is 1.5 μm and the lattice parameter is $d = 6$ μm along the [01] and [10] directions as defined in Fig. 1. The spatial design of the two patterns was motivated by the distinct magnetic response of the two element shapes. Using the phase shift of the circular islands between the two patterns (see Fig. 1) we have shown previously how it is

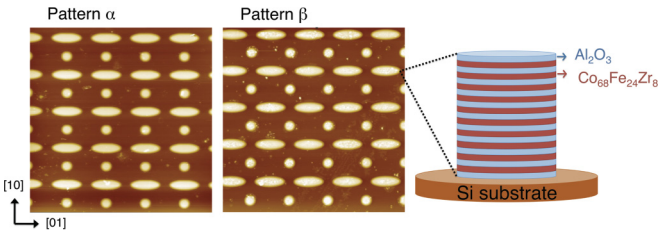

FIG. 1. (Color online) Atomic force microscopy images showing the patterned multilayers used in this investigation. The circular islands have a diameter of 1.5 μm and the ellipsoidal islands a 1.5 μm minor axis and a 4.5 μm major axis. The shortest distance between the edges of the islands is 1.5 μm resulting in a periodicity of $d = 6$ μm for both patterns α and β along both the [01] and [10] lattice directions.

possible to extract the individual magnetic responses of the two elements using diffracted magneto-optical measurements without resorting to arrays composed of single elements.[14] Extending diffraction methods from optical to x-ray energies allows shorter length scales to be accessed with the added advantage of element selectivity.[18–22]

B. X-ray resonant magnetic scattering

The XRMS measurements were performed on the ALICE two circle diffractometer[23] using circularly polarized photons at the undulator beamline UE56/2-PGM1 at the BESSY synchrotron. This beamline uses a plane grating monochromator with an energy resolution of about 100 meV in the 650–850 eV energy range and has a beam divergence of ~10 mrad. The exact degree of circular polarization produced depends on several factors but was approximately 85% for the data described here. The focused spot at the entrance to the experimental chamber was 90 μm (horizontal) and 200 μm (vertical).

A previous x-ray magnetic circular dichroism (XMCD) study on similar amorphous $Co_{68}Fe_{24}Zr_8$ layers recorded across the Co and Fe L_3 edges showed that the Co and Fe moments are ferromagnetically coupled.[24] Therefore, in this paper, we limit ourselves to a discussion on data recorded at an energy of $E = 777.0$ eV which is slightly below the Co L_3 resonance. At this energy the absorption is significantly reduced, compared to exactly on the resonance, and a larger penetration depth is achieved while still retaining the element-specific contrast from the real part of the magnetic scattering factor.[6] Due to the large observed resonant signal it was possible to record magnetization loops at different scattering conditions by measuring the scattered intensity as a function of an applied magnetic field using an *in situ* electromagnet.

The resonant electronic x-ray atomic scattering factor of a magnetic atom can be written within the dipole approximation as[25,26]

$$f(Q,E) = (\hat{\epsilon}_f \cdot \hat{\epsilon}_i)F^0(E) - i(\hat{\epsilon}_f \times \hat{\epsilon}_i) \cdot \hat{m}F^1(E). \quad (1)$$

Here E is the x-ray energy and Q the scattering vector defined in terms of the unit polarization vectors $\hat{\epsilon}_i$ and $\hat{\epsilon}_f$ which describe the incident and scattered x-rays, respectively. $\hat{m}$ is the magnetization unit vector which for the data described herein is assumed to be confined within the sample plane (see Fig. 2).

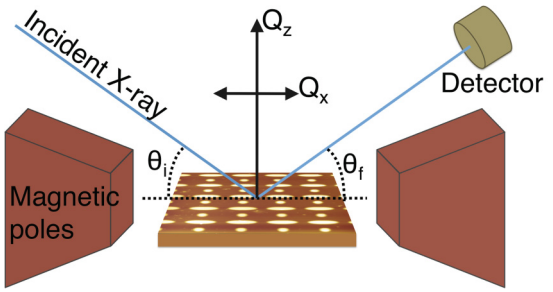

FIG. 2. (Color online) A schematic illustrating the scattering geometry. The magnetic field is applied in the plane of the sample. Through the selection of the sample angle θ_i and the detector angle θ_f the scattered intensity can be recorded as a function of the applied magnetic field at different points in reciprocal space.

$F^0(E) = f_0 + f'(E) + if''(E)$ is the charge-dependent scattering amplitude containing the atomic scattering factor f_0, as well as the real and imaginary parts of the anomalous scattering factor, f' and f''. The magnetic scattering amplitudes are contained in $F^1(E)$ and include the real, m', and imaginary, m'', parts of the complex magnetic scattering factor.[27] For low Q_z the scattering is sensitive to the in-plane components of the magnetization and proportional to the refractive index of the layers, $n = 1 - \delta^{\pm} + i\beta^{\pm}$ where $\delta^{\pm}(f_0 + f', \mp m')$ and $\beta^{\pm}(f'', \mp m'')$.

The recorded scattered intensity is proportional to the square of the total structure factor which contains interference terms between the magnetic and charge scattering amplitudes due to the different polarization dependence of the two terms in Eq. (1). This interference term can be obtained by measuring the asymmetry ratio

$$R = \frac{I^+ - I^-}{I^+ + I^-}, \quad (2)$$

where the scattered intensities I^+ and I^- are recorded for opposite saturation field directions under a fixed helicity, or for a fixed field value with reversed helicity.

The scattered intensity was recorded along the two orthogonal directions in reciprocal space defined in Fig. 2 (Q_z and Q_x). The scattering in Q_y was integrated using a wide acceptance slit in the xy plane. Specular scans which probe the sample structure perpendicular to the multilayer film (Q_z) are performed by moving the detector angle at twice the rate of the sample angle (i.e., $\theta_i = \theta_f$). The periodicity Λ of the multilayer in the out-of-plane direction gives rise to a series of low-angle Bragg peaks in the specularly reflected intensity at positions in reciprocal space given by $Q_z = 2\pi \times n/\Lambda$, where n is an integer. In-plane information from the sample is obtained by scanning the lateral scattering vector Q_x, which is probed by rocking the sample across the specular condition. To perform a true Q_x scan for a fixed value of Q_z the angle of the detector must be changed during the scan. For a rocking curve where the sample angle θ_i is changed with a fixed detector angle the relative change in the value of Q_z as the sample is rotated away from the specular condition towards the horizon ($\theta_i = 0$ or $\theta_i = 2\theta_f$) is given by $\frac{Q_z(\text{horizon})}{Q_z(\text{specular})} = \cos(\theta_f - \theta_i)$. For typical detector resolutions the change in Q_z as the sample is rocked close to the specular condition cannot be resolved so

the scan only depends on Q_x. Any in-plane periodicity in the x direction, d, arising from the lateral pattering of a sample will give rise to an additional series of diffraction peaks at $Q_x = 2\pi \times m/d$ where m is an integer. The accessible range of Q_x is limited by the experimental geometry and scales with the magnitude of Q_z.

III. RESULTS

A. Magneto-optical Kerr effect studies

The magnetization reversal of the patterned elements, averaged over the array, was studied using the magneto-optical Kerr effect (MOKE) in a longitudinal geometry[28] [Fig. 3(a)]. Further details regarding the MOKE study are given in Ref. 14. Due to the optical wavelengths used in MOKE, the technique is insensitive to the vertical periodicity of the multilayer. In this geometry the MOKE signal is only sensitive to the in-plane components of the magnetization with a depth sensitivity that scales with the amplitude of the electric field which decays exponentially into the material to a depth of ∼10 nm. The array was orientated such that the optical plane was coincident with the [01] axes which resulted in a series of diffracted light beams from the 6 μm periodicity on which MOKE analysis was performed.[14] As can be seen in Fig. 1 the difference between the two samples is a shift in the position of the circular islands with respect to the ellipsoidal island centers. Due to the large transverse coherence of the light beam in both the in-plane directions, this displacement causes an $e^{in\pi}$ phase shift in the scattering of the circles between the two samples. This results in an inversion of the circular island form factor for odd numbered diffraction orders for the two samples. The individual magnetization of the circular and ellipsoidal islands can therefore be obtained through the comparison of magnetization loops recorded for the two patterns at the first diffraction order. The diffracted MOKE results reveal a difference between the magnetization of the two island types when the field is applied along the easy [01] direction. The

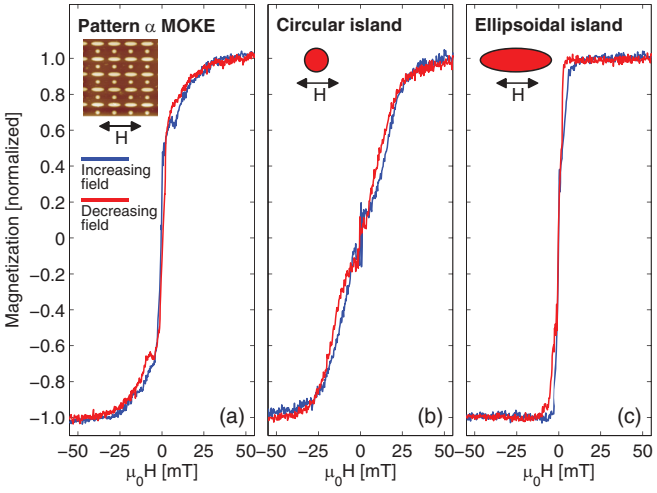

FIG. 3. (Color online) (a) MOKE magnetization loop for pattern α (pattern β showed similar results). (b, c) The normalized individual magnetization of the circular M_c and ellipsoidal M_e islands obtained by comparing MOKE magnetization loops recorded at the first diffraction order for the two patterns α and β (Ref. 14).

circular islands exhibit a hard magnetic transition extending up to $\mu_0 H \approx 30$ mT [Fig. 3(b)] while the ellipsoidal islands show a soft magnetic transition [Fig. 3(c)] at a lower switching field. Comparison between the MOKE data and micromagnetic simulations show that the saturation magnetization is the same for the two island types and that the island moment scales with the area (i.e., the ellipsoidal islands have a three times higher moment than the circular islands). For magnetic fields applied along the in-plane hard [10] direction both the circular and ellipsoidal islands exhibit a similar field dependence with comparable saturation field values and the field dependence of the two elements cannot be distinguished easily.[14]

B. X-ray reflectivity

We first begin our presentation of the resonant magnetic scattering data by considering the specular scattering. Due to the much shorter wavelength of the x-ray probe compared with the optical MOKE measurements the x-ray data are sensitive to both the in-plane array spacing and the out-of-plane multilayer structure. At the specular condition the in-plane component of the scattering vector is zero ($Q_x = 0$) and hence insensitive to any in-plane structure. Thus, even though the sample is composed of a laterally patterned array of circular and ellipsoidal islands which exhibit different magnetic responses, the specular data record an in-plane average of the field responses of the two elements.

The specular scattering intensity was recorded as a function of Q_z using a fixed helicity for all samples. At each point on the reflectivity curve the intensity was measured under reversed saturating fields of ±110 mT. The electromagnet followed the sample axis ensuring that the field was applied in-plane.[23] The resulting intensities ($I^{\pm}$) and the asymmetry ratio R for pattern α are shown in Fig. 4. There was no significant change in the specular data for different azimuth angles and both patterns showed similar reflectivity and asymmetry ratio profiles.

Unlike MOKE, the specular XRMS data show a clear dependence on Q_z due to their sensitivity to the out-of-plane structure. Bragg peaks observed up to the fourth order and the presence of total thickness oscillations (Kiessig fringes) in the specular scattering (Fig. 4) indicate a well-defined layered structure and that the x-rays penetrate to the bottom of the ∼63 nm thick multilayer. The asymmetry ratio is shown in Fig. 4(b). It remains positive over the entire range of Q_z probed and shows peaks at the Bragg positions. These peaks are more clearly defined in the difference spectrum which has been scaled by Q_z^4 and is shown in Fig. 4(c). There is no indication of a magnetic dead-layer at the interface between the $Co_{68}Fe_{24}Zr_8$ and Al_2O_3 layers as there is no additional interference term modulating the magnetic peak intensities or the overall asymmetry ratio as a function of Q_z.[29] The out-of-plane electronic and magnetic profile was determined assuming continuous layers and simultaneously fitting the two specular data sets using the GENX code.[30] The resultant best-fit curves are shown for all data sets in Fig. 4. As the GENX code is fully dynamical, refraction effects are taken into account in the simulations. From the fits to the charge and magnetic profiles (black lines in Fig. 4) the multilayer periodicity was determined to be $\Lambda = 6.06 \pm 0.01$ nm in agreement with the nominal growth parameters and data recorded at 8.8 keV.[14]

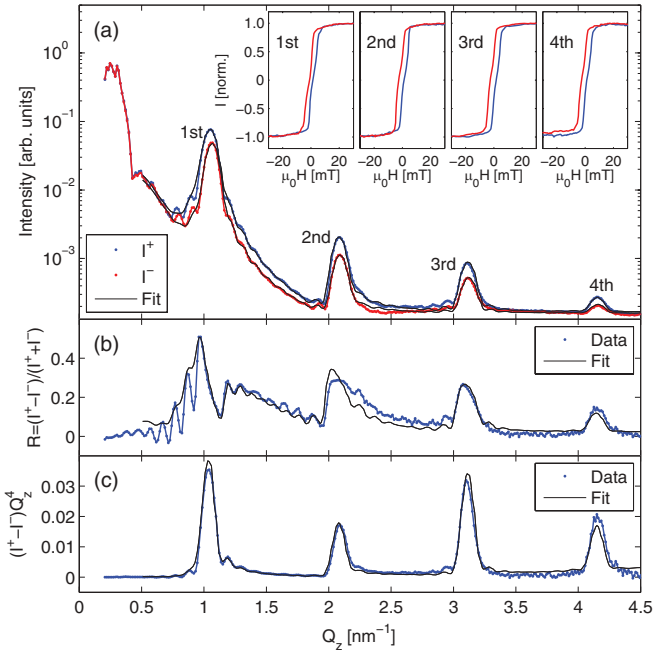

FIG. 4. (Color online) (a) Specular reflectivity recorded for opposite saturation fields ($I^{\pm}$) for pattern α. The insets show magnetization loops recorded at each of the four multilayer Bragg peaks. (b) Asymmetry ratio $R = (I^+ - I^-)/(I^+ + I^-)$ as a function of Q_z. A slight shift in the position of the first multilayer Bragg peak is seen between the two reflectivity scans which results in the observed asymmetry. (c) The difference signal scaled by Q_z^4 [i.e., $(I^+ - I^-)Q_z^4$]. Clear magnetic signals are seen at the Bragg peak positions. Best fits to the data derived by simultaneous fitting of the spectra shown in (a) are shown as lines.

With the sensitivity to the magnetic profile the thicknesses of the individual layers were determined to high precision to be $d_{Co_{68}Fe_{24}Zr_8} = 3.27 \pm 0.01$ nm and $d_{Al_2O_3} = 2.79 \pm 0.01$ nm. The fitted magnetic profile within the $Co_{68}Fe_{24}Zr_8$ layer correlates exactly with the chemical profile. The interface roughness for the chemical and magnetic profiles of the $Al_2O_3/Co_{68}Fe_{24}Zr_8$ interface were 0.69 ± 0.01 nm while a smoother $Co_{68}Fe_{24}Zr_8/Al_2O_3$ interface of 0.27 ± 0.01 nm was observed. As a consequence of allowing the resonant scattering terms to vary in the model, only the relative moment of the $Co_{68}Fe_{24}Zr_8$ magnetic layers was extracted. No variation of the moment was observed between the layers as the sample was saturated under each reversed field and all the individual layers therefore show the same structural and magnetic properties.

X-ray scattering measurements are always susceptible to absorption and refraction. The effect is limited when using hard x-ray energies but can become significant when the energy is tuned close to a resonance condition. It can be further exacerbated when conducting resonant magnetic scattering from the transition metals as the direct dipole transitions occur at the soft $L_{2,3}$ edges. Under such circumstances, the refractive index of the layers in the structure can be significantly different for x-rays of opposite helicity or under reversed applied saturation fields due to the influence of the magnetic scattering amplitudes. This can give rise to dynamical effects in the scattered intensity at low Q_z such as shifts in peak positions[31] and a smearing of the critical angle. In our data such dynamical effects are clearly observed. The position of the first Bragg peak in Fig. 4(a) is shifted in the reflectivity channels corresponding to the two opposing saturation field directions. For higher scattering angles the dynamical effect is reduced and higher-order Bragg peaks show no shift in position. The effect can also be observed in the asymmetry ratio shown in Fig. 4(b) which is predominantly positive over the entire recorded specular scan. For $Q_z \lesssim 0.5$ nm^{-1} the asymmetry is zero as the reflectivity comes predominantly from the Si substrate and there is no magnetic signal. For higher values of Q_z the asymmetry ratio exhibits oscillations with a periodicity corresponding to the Kiessig fringes in the reflectivity. No clear first-order Bragg peak is seen in the asymmetry ratio (at $Q_z \approx 1$ nm^{-1}), but a sharp feature can be seen that is associated with the shifted position of the first-order Bragg peak in the two reflectivity channels which introduces a modulation in the asymmetry ratio at this position.

The effect of refraction can be corrected for by considering the scattering from the perspective of the internal reciprocal lattice vector Q^*. Multilayer Bragg diffraction will occur when Q_z^* satisfies the condition[32]

$$Q_z^* = \frac{2\pi}{\lambda}\left(\sin\theta_i + \left[\left\{\frac{m\lambda}{\Lambda} - (\sin^2\theta_i - \sin^2\theta_c)^{1/2}\right\}^2 + \sin^2\theta_c\right]^{1/2}\right). \quad (3)$$

Fitting this equation to the positions of the observed Bragg peaks in the reflectivity curves shown in Fig. 4(a) enables the critical angles $\theta_c^{\pm}$ for each of the field directions to be determined.[33] For the positive saturation field a critical angle of $\theta_c^+ = 1.23 \pm 0.03^\circ$ is found whereas for the negative saturation field a value of $\theta_c^- = 1.70 \pm 0.03^\circ$ is obtained, clearly showing that the near surface material is ferromagnetic. Using the values for θ_c^+ and θ_c^- the two reflectivity curves in Fig. 4 can be corrected for the effects of refraction using Eq. (3), resulting in the curves shown in Fig. 5. After correction, multilayer Bragg peaks are uniformly spaced in Q_z^* and are aligned for the two field directions. The modulations observed in the uncorrected asymmetry ratio at low Q_z have been removed and the corrected asymmetry ratio is a smoothly varying function.

C. Magnetization reversal

Unlike MOKE measurements which have no sensitivity to the out-of-plane structure, recording the scattered XRMS intensity as a function of magnetic field at specific points in reciprocal space probes the magnetization reversal along different projections. Magnetization loops recorded at the first four specular Bragg peaks are shown as insets in Fig. 4. These loops record the average in-plane x component of the Co moments which have the same vertical periodicity as the $Co_{68}Fe_{24}Zr_8/Al_2O_3$ bilayers. As all four loops are similar we conclude that the magnetic profile is uniform through the $Co_{68}Fe_{24}Zr_8$ layer, in agreement with the best fit profile shown in Fig. 4. Similar magnetization loops were obtained at the Bragg peaks for both patterns α and β. The similarity of the loops between the two patterns indicates that dipole coupling between the circular and ellipsoidal islands is limited and does

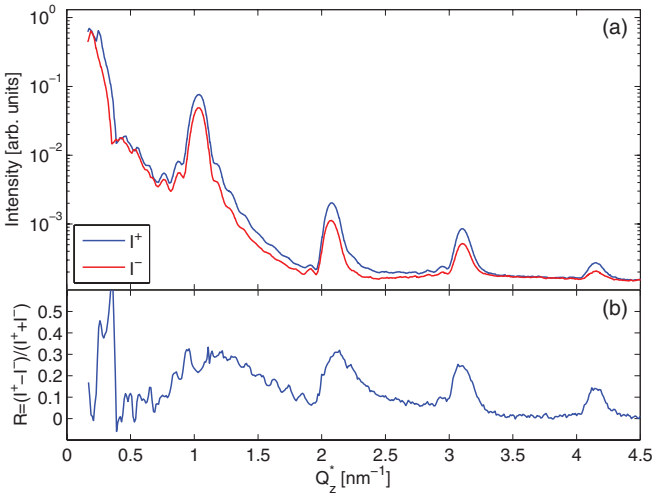

FIG. 5. (Color online) (a) Specular reflectivity and (b) asymmetry ratio for pattern α after correcting for the refractive index for the two different saturation magnetization directions.

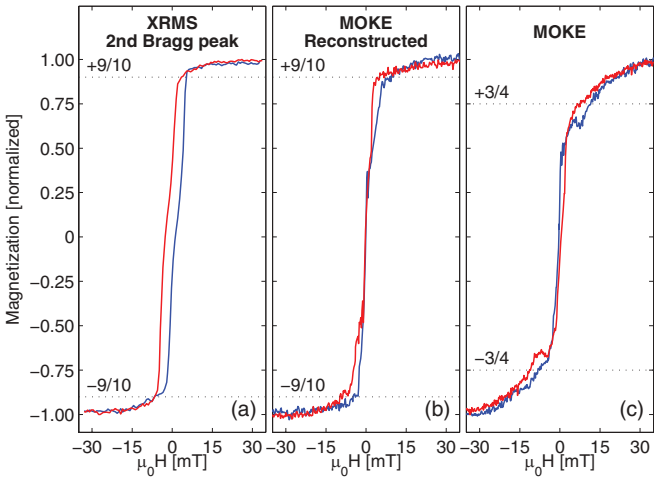

FIG. 6. (Color online) (a) Magnetization loop recorded using XRMS on the second multilayer Bragg peak for pattern α. (b) Magnetization loop reconstructed from the individual magnetizations of the circular and ellipsoidal islands obtained from diffracted MOKE using Eq. (5). (c) MOKE magnetization loop.

not depend on the lattice geometry. All four magnetization loops exhibit similar magnetization reversal characteristics, but the loop at the first Bragg peak has a slightly reduced coercivity. This apparent change in behavior is an artifact due to the refractive index changes that occur when the magnetization is reversed. As the hysteresis loops are recorded at a fixed external Q_z position not only does the intensity change abruptly due to the changed magnetic state, but there is also an intensity change associated with the concomitant shift of the Bragg peak position when the magnetic layers reverse. As seen in Fig. 4(b) the effect is more pronounced at lower Q_z.

Although the magnetization loops measured using MOKE and XRMS (recorded at the multilayer Bragg peak Q_z positions) probe the same average magnetization they show different behavior. The magnetization loop recorded at the second multilayer Bragg peak (Fig. 4) is displayed in Fig. 6(a). The clear difference between this XRMS loop and the MOKE loop is evident in Fig. 6(c). As the area of the ellipsoidal islands is three times larger than the area of the circular islands the total magnetic signal from the ellipsoidal islands corresponds to 3/4 of the observed total magnetization and the signal from the circular islands the remaining 1/4. This simple ratio is seen in the weighting in the MOKE loops, but for the XRMS loops recorded at the specular Bragg peaks this ratio is clearly altered. In the XRMS data the contribution of the circular islands is now reduced at the expense of the ellipsoidal island transition.

For a multilayer consisting of repetitions of equally thick bilayers A and B the scattered intensity at the specular nth Bragg condition scales with the difference in the scattering amplitude of the two layers through

$$I(n) \propto |f_A(n) - f_B(n)|^2, \tag{4}$$

where $f_A(n)$ is the total scattering factor for layer A and similarly for layer B. Assuming that the charge scattering, f^0 and anomalous terms f' and if'' are not affected by the magnetic state of the material, they can be neglected and only the complex magnetic scattering form factor $m' + im''$ needs to be considered when investigating the field response of the multilayer structures. Assuming layer B to be nonmagnetic, the scattered intensity as a function of applied field at a fixed value of Q_z corresponding to a Bragg peak position is then given by $I(n,H) = |f_A^{\mathrm{mag}}(n,H)|^2$. For the patterns described here, the magnetic scattering intensity on a specular Bragg peak from the patterned multilayers as a function of an applied field at the Bragg condition follows to first order

$$I^{\mathrm{mag}} \propto M_c(H)^2 a_c^2 + M_e(H)^2 a_e^2, \tag{5}$$

resulting in a contribution to the observed magnetization of 1/10 for the circular islands and a ratio of 9/10 for the ellipsoidal islands given their larger area.

The shape of the XRMS loop [Fig. 6(a)] can be reproduced [Fig. 6(b)] using the extracted normalized individual magnetization loops determined from diffracted MOKE (shown in Fig. 3) as the functions $M_c(H)$ and $M_e(H)$ in Eq. (5). The differences between Figs. 6(a) and 6(b) may be ascribed to the different penetration depths of the two probes. MOKE measures a magnetic signal which is independent of the vertical sample structure and simply integrates over the sampling depth with a weight factor that decays exponentially into the sample. This is highlighted by the observation of an inverted coercivity in the specularly reflected MOKE magnetization loops. XRMS has a greater overall penetration depth, and as can be seen in Fig. 4 samples the entire vertical extent. The data in Fig. 6(a) are recorded on a specular Bragg peak, the intensity of which is related both to the magnetization direction within the bilayers and their vertical correlation. These combined effects result in the observation of a higher coercivity in agreement with the micromagnetic simulations as discussed in Ref. 14.

D. Off-specular scattering

The effect of the patterned elements on the observed magnetization reversal recorded in the specular condition is

clear in the data shown in Fig. 6. However, the effect of the lateral periodicity on the magnetic scattering can only be investigated by moving away from the specular condition. With an in-plane component to the scattering vector and a suitably large coherence length the scans are sensitive to the interface morphology through the diffuse scattering as well as any in-plane periodicity. For synchrotron radiation the transverse coherence length in the Q_x direction is usually of the order of tens of micrometers leading to a much larger projected coherence at low angles. The coherence of the incident beam in the Q_y direction is much lower, typically of the order of a micron, and coupled with the instrument resolution the data described here are insensitive to the array periodicity in the y direction. The phase sensitivity to the different spatial distributions of the two patterns α and β is therefore lost. In the XRMS data we observed no clear differences between the patterned samples. A similar analysis as in the diffracted MOKE study,[14] where the transverse coherence of the beam is large in both Q_y and Q_x, can therefore not be performed.

The large transverse coherence length in the Q_x direction, however, gives rise to clear diffraction peaks due to the periodicity of the patterns in the xz plane with the elements scattering in phase.[34] The low coherence in the Q_y direction means that the scattering from these arrays can be considered to be the intensity sum of a series of circular and ellipsoidal rows (Fig. 1). As the coherence length along the rows is large the scattering amplitude for each row includes the form factor for the element type and appropriate phase factors. Away from the specular multilayer Bragg peaks the scattering from the rows is therefore weighted by the element area and is given by

$$I(Q,H) = a_c \left| \int^N f(Q,M_c) F_c(x,y,H) e^{(iQx)} dx \right|^2 + a_e \left| \int^N f(Q,M_e) F_e(x,y,H) e^{(iQx)} dx \right|^2, \quad (6)$$

where $F_c(x,y,H)$ and $F_e(x,y,H)$ are the in-plane form factors for the elements and describe their charge and magnetic shapes and N is the number of coherently illuminated elements in the x direction.

We begin the discussion of the off-specular data by considering a rocking curve recorded at a Q_z value corresponding to the first specular Bragg peak. At this Q_z position the diffuse scattering is proportional to correlations in the interface disorder that extend over the bi-layer repeat distance. Rocking curves taken with opposite saturation fields are shown in Fig. 7(a). As expected the individual scans are peaked at the specular condition and the diffuse scattering shows a distribution characteristic of correlated roughness with a large in-plane correlation length ξ_x. This length scale can be estimated from the full width at half maximum of the diffuse peak $\xi_x \approx 2\pi/\Delta(Q_x) \approx 2\,\mu$m and is of the same order as the cutoff length scale introduced by the element size. The difference signal shown in Fig. 7(b) shows a similarly broad peak in Q_x suggesting that the magnetic distribution has a similar in-plane correlation length under saturating conditions to the charge morphology. The two intensity curves show different Q_x scaling in the peak tails which is further

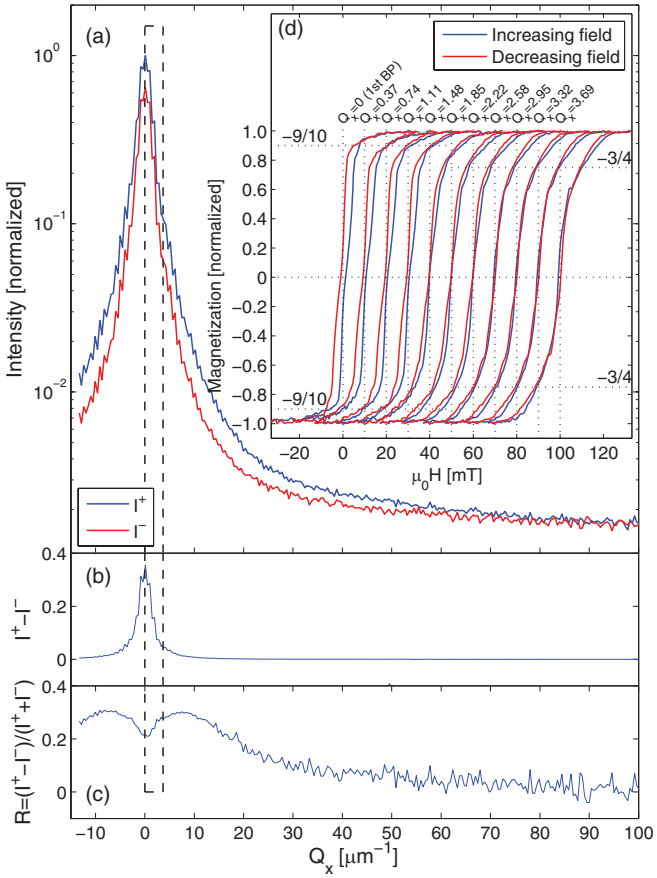

FIG. 7. (Color online) (a) Q_x scan recorded around the first multilayer Bragg peak ($Q_z = 1.04$ nm^{-1}), (b) the difference signal, and (c) the asymmetry ratio of the scattered intensity. The dip in the asymmetry ratio occurs along with the onset of the specular condition. The dashed lines indicate the part of the curve where hysteresis loops were recorded. (d) Magnetization loops recorded within the dashed area. The magnetization loop recorded at $Q_x = 0$ corresponds to the center of the multilayer Bragg peak. The consecutive loops, recorded by shifting Q_x by 0.37 μm^{-1}, are shifted in the graph by 10 mT to illustrate their evolution as a function of Q_x.

highlighted in the asymmetry ratio shown in Fig. 7(c). It is difficult to interpret directly the shape of the asymmetry ratio in this region due to the refraction effects highlighted above and the complex interplay between the magnetic and charge scattering factors as well as the diffuse scattering coming from the correlated interface morphology.

Magnetization loops [Fig. 7(d)] were recorded along the rocking curve from the Bragg condition at intervals of $\Delta Q_x = 0.37\,\mu$m^{-1}. As the Q_x value changes and the scattering vector moves away from the Bragg peak a clear evolution in the shape of the magnetization loops is observed. A reduction of the apparent coercivity as well as a change in the behavior of the magnetization towards saturation is seen as a function of Q_x. Away from the specular condition the form factors and in-plane distribution of the elements affect the intensity of the scattering and a similarity with the MOKE magnetization loops (Fig. 3) is observed at high Q_x. At $Q_x \geqslant 2.58\ \mu$m^{-1} a negative hysteresis is invoked as was also seen in the MOKE loops. The negative hysteresis occurs due to

the absorption of the beam, giving preferential weighting to the uppermost layers, which have a different apparent interlayer coupling due to the demagnetizing fields from the lower-lying layers.[14]

The periodic structure of the pattern gives rise to in-plane diffraction peaks at $Q_x = 2\pi \times m/d$. Since the periodicity of the patterning is large these diffraction peaks are only observed at low Q_x values. On close inspection of Fig. 7(a) these peaks can be seen as steps in the data, but are at the limit of the experimental resolution. To improve the Q_x resolution rocking curves can be recorded at lower detector angles. Away from the Bragg peak the diffuse scattering only originates from the uncorrelated components of the interface morphology which is significantly reduced in these samples further enhancing the visibility of the in-plane diffraction peaks. Figure 8(a) shows a rocking scan for pattern α recorded at $Q_z = 0.33$ nm^{-1} with the beam and the applied magnetic field aligned along the [01] direction. The data display clear diffraction peaks with the appropriate spacing in Q_x, which corresponds to the 6 μm periodicity in real space. As before, the difference signal and asymmetry ratio R, are obtained by measuring the intensity under opposite saturation fields [Figs. 8(b) and 8(c)] and reveal the variations of the intensities due to the different phase contributions of the array elements. Although convolutions between the lateral and vertical scattering components cannot be ignored, the magnetic signal shown in Fig. 8(c) is dominated by the lateral form factors of the pattern which introduces a modulation of the asymmetry ratio with a periodicity corresponding to a length scale comparable to the diameter of the circular islands.[35]

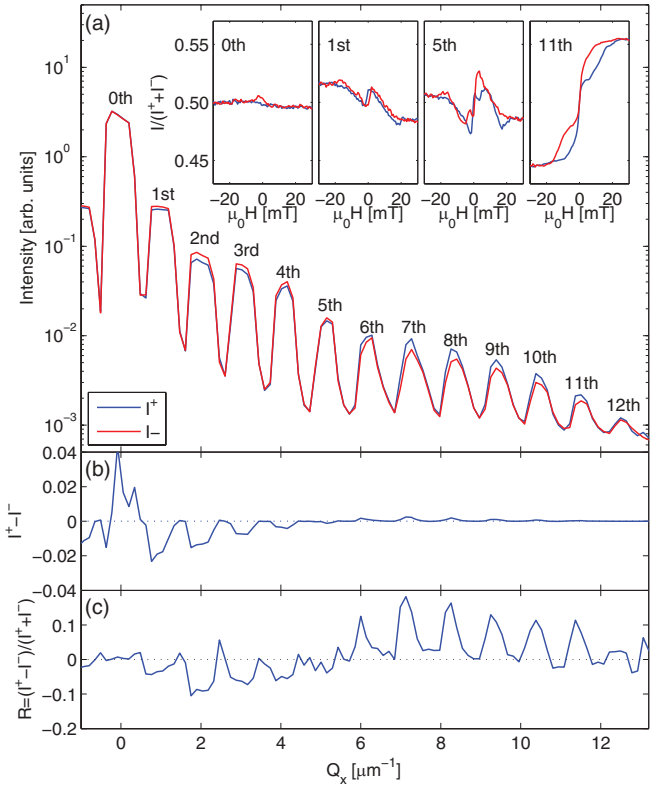

FIG. 8. (Color online) (a) Q_x scan along the [01] direction, (b) difference signal, and (c) the asymmetry ratio recorded for opposite saturation magnetization for pattern α around $Q_z = 0.33$ nm^{-1}. The insets show magnetization loops [scaled with respect to $(I^+ + I^-)$] recorded at the specular condition (zeroth) and the first, fifth, and 11th diffraction peaks observed in the scan.

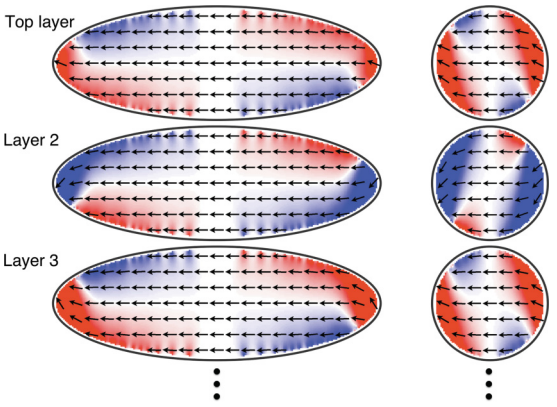

FIG. 9. (Color online) Results of micromagnetic calculations for the top three layers of the ellipsoidal and circular islands for an applied magnetic field of $\mu_0 H = -15$ mT along the lateral direction. Dipole interactions between layers at the edges of the structures affect the magnetization distribution within the layers resulting in divergences at the apexes of the elements. The arrows indicate the direction of the magnetization vector and the red and blue contrast displays its y component.

By recording magnetization loops at diffraction peaks information about the magnetization distribution of the array and within the structures can be obtained as smaller length scales are probed for higher diffraction orders. The insets in Fig. 8(a) show magnetization loops recorded at selected positions in the Q_x scan. As in the MOKE analysis two switching mechanisms are observed, a soft switching mechanism at small fields attributed to the ellipsoidal islands and a harder switching mechanism extending up to higher fields attributed to the circular islands. The relative and absolute intensities of these two components change as a function of diffraction order due to the form factors of the circular and ellipsoidal islands. Although the coherence length in Q_y is small, it is finite and the scattering is sensitive to the element shape in the y direction. At the highest diffraction orders where the smallest length scales are probed the curvature of the elements becomes important. Figure 9 shows the results of micromagnetic calculations[14] for the top three layers of both the circular and ellipsoidal islands. The calculations reveal the magnetization for each layer to deviate from a single domain state and display divergences due to the dipole interaction between the layers. When seen at a sufficiently small length scale these divergences are enhanced, affecting the shape of the magnetization loop recorded at high diffraction orders such as the 11th order magnetization loop shown in Fig. 8(a).

IV. CONCLUSIONS

By using soft x-ray resonant magnetic scattering it is possible to characterize the material structure and element specific magnetic arrangement of patterned multilayer structures

over a wide range of length scales. By choosing appropriate scans and probing specific points in reciprocal space both the in-plane and out-of-plane chemical and magnetic profiles can be elucidated. From MOKE measurements and micromagnetic simulations the magnetization reversal is well understood in our samples. This allows us to develop new insights into the convolution of the scattered intensity with the underlying structural and magnetic configurations. Using the distinct magnetic response of the two element shapes their magnetic scattering intensity, recorded at the specular Bragg condition, was found to scale with the square of the surface area. Altering the magnetic state of the material modifies the refractive index of the layers influencing the scattering amplitudes. Such effects are enhanced at low angles where changes in the refractive index need to be corrected to obtain data which can be compared directly with MOKE and other bulk probes of the magnetization. As the coherence length of the x-rays in the Q_x direction is larger than the in-plane periodicity, the scattering for the array elements will interfere, resulting in phase relations that depend on the scattering geometry. The observed magnetic scattering and magnetization loops recorded with an in-plane component, both at and away from the specular Bragg peak positions, is modulated by the phase contributions of the different elements in the array affecting the interpretation of the results. Further development in codes for describing the scattering process would open up the possibilities of studying three-dimensionally patterned structures with greater detail in a wide range of length scales in all spatial dimensions.

ACKNOWLEDGMENTS

The authors would like to acknowledge the support of the Swedish Research Council (VR) and the Knut and Alice Wallenberg Foundation (KAW) and funding from the Icelandic Nanoscience and Nanotechnology program and the Icelandic Research Fund for Graduate Students. We thank Matts Björck for useful discussions. This work was partially supported by the UK EPSRC through the Spin@RT consortium. The ALICE project is supported by the BMBF Contract No. 05K10PC2. We acknowledge support from the HZB facility in Berlin.

[1] A. Zvezdin and V. Kotov, *Modern Magnetooptics and Magnetooptical Materials* (IOP, London, 1997).
[2] C. Kao, J. B. Hastings, E. D. Johnson, D. P. Siddons, G. C. Smith, and G. A. Prinz, Phys. Rev. Lett. **65**, 373 (1990).
[3] H. A. Durr, T. Eimuller, H.-J. Elmers, S. Eisebitt, M. Farle, W. Kuch, F. Matthes, M. Martins, N.-C. Mertins, P. M. Oppeneer, L. Plucinski, C. M. Schneider, H. Wende, W. Wurth, and H. Zabel, IEEE Trans. Magn. **45**, 15 (2009).
[4] J. M. Tonnerre, L. Sève, D. Raoux, G. Soullié, B. Rodmacq, and P. Wolfers, Phys. Rev. Lett. **75**, 740 (1995).
[5] T. P. A. Hase, I. Pape, B. K. Tanner, H. Durr, E. Dudzik, G. van der Laan, C. H. Marrows, and B. J. Hickey, Phys. Rev. B **61**, R3792 (2000).
[6] C. Spezzani, P. Torelli, M. Sacchi, R. Delaunay, C. F. Hague, F. Salmassi, and E. M. Gullikson, Phys. Rev. B **66**, 052408 (2002).
[7] Y. U. Idzerda, V. Chakarian, and J. W. Freeland, Phys. Rev. Lett. **82**, 1562 (1999).
[8] C. H. Marrows, P. Steadman, A. C. Hampson, L.-A. Michez, B. J. Hickey, N. D. Telling, D. A. Arena, J. Dvorak, and S. Langridge, Phys. Rev. B **72**, 024421 (2005).
[9] J. I. Martín, J. Nogués, K. Liu, J. L. Vicent, and I. K. Schuller, J. Magn. Magn. Mater. **256**, 449 (2003).
[10] A. O. Adeyeye and N. Singh, J. Phys. D: Appl. Phys. **41**, 153001 (2008).
[11] O. Geoffroy, D. Givord, Y. Otani, B. Pannetier, A. D. Santos, M. Schlenker, and Y. Souche, J. Magn. Magn. Mater. **121**, 516 (1993).
[12] M. Grimsditch and P. Vavassori, J. Phys.: Condens. Matter **16**, R275 (2004).
[13] A. Westphalen, M.-S. Lee, A. Remhof, and H. Zabel, Rev. Sci. Instrum. **78**, 121301 (2007).
[14] U. B. Arnalds, E. T. Papaioannou, T. P. A. Hase, H. Raanaei, G. Andersson, T. R. Charlton, S. Langridge, and B. Hjörvarsson, Phys. Rev. B **82**, 144434 (2010).
[15] H. Raanaei, H. Nguyen, G. Andersson, H. Lidbaum, P. Korelis, K. Leifer, and B. Hjörvarsson, J. Appl. Phys. **106**, 023918 (2009).
[16] H. Lidbaum, H. Raanaei, E. T. Papaioannou, K. Leifer, and B. Hjörvarsson, J. Cryst. Growth **312**, 580 (2010).
[17] A. Liebig, P. T. Korelis, H. Lidbaum, G. Andersson, K. Leifer, and B. Hjörvarsson, Phys. Rev. B **75**, 214202 (2007).
[18] G. van der Laan, C. R. Phys. **9**, 570 (2008).
[19] G. van der Laan, Curr. Opin. Solid State Mater. Sci. **10**, 120 (2006).
[20] K. Chesnel, M. Belakhovsky, S. Landis, B. Rodmacq, J. C. Toussaint, S. P. Collins, G. van der Laan, E. Dudzik, and S. S. Dhesi, Phys. Rev. B **66**, 024435 (2002).
[21] D. R. Lee, J. W. Freeland, Y. Choi, G. Srajer, V. Metlushko, and B. Ilic, Phys. Rev. B **76**, 144425 (2007).
[22] D. S. Eastwood, T. P. A. Hase, M. van Kampen, R. Brucas, B. Hjörvarsson, D. Atkinson, and B. K. Tanner, Superlattices Microstruct. **41**, 163 (2007).
[23] J. Grabis, A. Nefedov, and H. Zabel, Rev. Sci. Instrum. **74**, 4048 (2003).
[24] T. Hase, H. Raanaei, H. Lidbaum, C. Sánchez-Hanke, S. Wilkins, K. Leifer, and B. Hjörvarsson, Phys. Rev. B **80**, 134402 (2009).
[25] J. P. Hannon, G. T. Trammell, M. Blume, and D. Gibbs, Phys. Rev. Lett. **61**, 1245 (1988).
[26] M. Abes, D. Atkinson, B. K. Tanner, T. R. Charlton, S. Langridge, T. P. A. Hase, M. Ali, C. H. Marrows, B. J. Hickey, A. Neudert, R. J. Hicken, D. Arena, S. B. Wilkins, A. Mirone, and S. Lebègue, Phys. Rev. B **82**, 184412 (2010).
[27] J. P. Hill and D. F. McMorrow, Acta Crystallogr. Sect. A **52**, 236 (1996).
[28] E. T. Papaioannou, V. Kapaklis, P. Patoka, M. Giersig, P. Fumagalli, A. Garcia-Martin, E. Ferreiro-Vila, and G. Ctistis, Phys. Rev. B **81**, 054424 (2010).
[29] N. Ishimatsu, H. Hashizume, S. Hamada, N. Hosoito, C. S. Nelson, C. T. Venkataraman, G. Srajer, and J. C. Lang, Phys. Rev. B **60**, 9596 (1999).
[30] M. Björck and G. Andersson, J. Appl. Crystallogr. **40**, 1174 (2007).
[31] S. M. Valvidares, C. Quirós, A. Mirone, J.-M. Tonnerre, S. Stanescu, P. Bencok, Y. Souche, L. Zárate, J. I. Martín, M. Vélez, N. B. Brookes, and J. M. Alameda, Phys. Rev. B **78**, 064406 (2008).

[32]P. Busch, M. Rauscher, D.-M. Smilgies, D. Posselt, and C. M. Papadakis, J. Appl. Crystallogr. **39**, 433 (2006).

[33]I. Hughes and T. Hase, *Measurements and Their Uncertainties - A Practical Guide to Modern Error Analysis* (Oxford University Press, New York, 2010).

[34]G. Beutier, A. Marty, F. Livet, G. van der Laan, S. Stanescu, and P. Bencok, Rev. Sci. Instrum. **78**, 093901 (2007).

[35]U. B. Arnalds, T. P. A. Hase, E. T. Papaioannou, H. Raanaei, R. Abrudan, T. R. Charlton, S. Langridge, and B. Hjörvarsson, (unpublished).